

# Computational modeling and neutron imaging to understand interface shape and solute segregation during the vertical gradient freeze growth of BaBrCl:Eu



Jeffrey J. Derby<sup>a,\*</sup>, Chang Zhang<sup>a</sup>, Jan Seebeck<sup>a</sup>, Jeffrey H. Peterson<sup>a</sup>, Anton S. Tremsin<sup>b</sup>, Didier Perrodin<sup>c</sup>, Gregory A. Bizarri<sup>c</sup>, Edith D. Bourret<sup>c</sup>, Adrian S. Losko<sup>d</sup>, Sven C. Vogel<sup>d</sup>

<sup>a</sup> Department of Chemical Engineering and Materials Science, University of Minnesota, Minneapolis, MN 55455, USA

<sup>b</sup> Space Sciences Laboratory, University of California at Berkeley, Berkeley, CA 94720, USA

<sup>c</sup> Lawrence Berkeley National Laboratory, Berkeley, CA 94720, USA

<sup>d</sup> Los Alamos National Laboratory, Los Alamos, NM 87545, USA

## ARTICLE INFO

Communicated by Chung wen Lan

### Keywords:

A1. Computer simulation  
A1. Heat transfer  
A1. Segregation  
A1. Neutron imaging  
A2. Bridgman technique  
B2. Scintillator materials

## ABSTRACT

We apply continuum models to analyze phase change, heat transfer, fluid flow, solute transport, and segregation in order to understand prior neutron imaging observations of the vertical gradient freeze growth of Eu-doped BaBrCl. The models provide a rigorous framework in which to understand the mechanisms that are responsible for the complicated evolution of interface shape and dopant distribution in the growth experiment. We explain how a transition in the solid/liquid interface shape from concave to convex is driven by changes in radial heat transfer caused by furnace design. We also provide a mechanistic explanation of how dynamic growth conditions and changes of the flow structure in the melt result in complicated segregation patterns in this system. A growth pause caused by controller lock-up is shown to result in a band of solute depletion in accordance with classical theory. However, changing flow patterns during growth result in a non-monotonic axial distribution of solute that cannot be explained by simple application of classical segregation models. We assert that the approach presented here, namely the use of rigorous models in conjunction advanced diagnostics, such as neutron imaging, provides an exciting path forward for process optimization and control, accelerating the incremental advances that have, in the past, typically relied on empiricism, experience, and intuition.

## 1. Introduction

The growth of large, single crystals of inorganic compounds from the melt has always presented significant technical challenges due to the need for very high temperatures, spanning the melting point of the material, and very long process times that arise from the slow rates required for stable growth. One of the earliest melt growth techniques was developed by Bridgman [1,2] and involved the withdrawal of an ampoule containing a charge from a high-temperature furnace. According to the excellent historical overview presented by Feigelson [3], Tammann [4] and Obreimov and Schubnikov [5], in work concurrent with that of Bridgman, grew bulk single crystals via a powering down of the furnace, effectively moving the thermal profile rather than the charge itself, in a process now referred to as the vertical gradient freeze method (VGF). Bridgman's method for directional solidification was later significantly refined by Stockbarger [6], who used two,

independently controlled furnaces separated by a zone to achieve crystal growth more reproducibly and under well-defined axial temperature gradients. The Bridgman, Bridgman-Stockbarger, and VGF processes have since been widely employed to grow a myriad of different crystals.

However, since their inception nearly a century ago, a significant challenge to the operation and understanding of these directional solidification processes is the near absence of any diagnostic tools available to directly monitor crystal growth. Direct observation of growth in these systems is hindered by the opaque, refractory materials typically required for high-temperature operation and the tight spacing between the ampoule and furnace bore. Rather, only indirect measures, such as temperatures at selected points within the furnace, have typically been employed for logging and control of the process. In fact, most of our observations of the workings within a directional solidification system are inferred *a posteriori*, using measures of the outcomes of a completed

\* Corresponding author.

E-mail address: [derby@umn.edu](mailto:derby@umn.edu) (J.J. Derby).

<https://doi.org/10.1016/j.jcrysgr.2020.125572>

Received 17 February 2020; Accepted 22 February 2020

Available online 27 February 2020

0022-0248/© 2020 Elsevier B.V. All rights reserved.

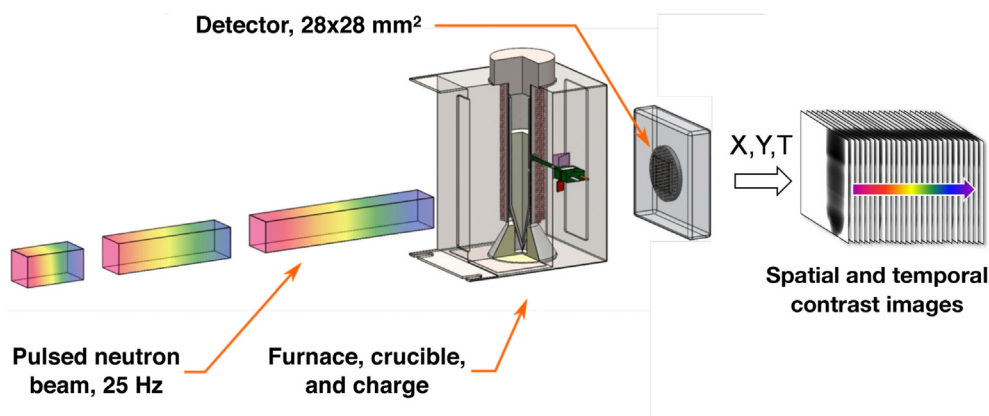


Fig. 1. Schematic diagram of the neutron imaging system for the vertical gradient freeze (VGF) growth of BaBrCl:Eu. Details of this system and initial experiments are described Refs. [58,59].

crystal growth run, such as interface shapes inferred via compositional striations induced by inherent or forced growth rate variations [7–12], measures of the global compositional field in the grown crystal [13–15], or observations of interface shapes after growth runs have been quenched [16,17]. Such comparisons are not completely satisfactory, because they do not reveal the actual state of the crystal as it grows. Furthermore, such post-growth measures often require the destruction of the crystal, making such characterization difficult and expensive. Hence, Bridgman growth has historically been conducted blindly, in the absence of meaningful, real-time diagnostics.

A variety of approaches have been attempted to directly observe bulk crystal growth in directional solidification systems. Wilcox and co-workers [18,19] were among the first to employ a transparent furnace to study phase change in a vertical Bridgman–Stockbarger system, using naphthalene and salol as model systems. Singh et al. [20] designed a transparent, multi-heating zone furnace for the growth of lead bromide. Lan et al. [21–23] developed a transparent furnace for crystal growth and flow visualization of sodium nitrate. Later, Batur et al. [24,25] implemented control schemes that relied upon the direct observation of the melt–crystal interface with a video camera and real-time imaging software. Since then, transparent furnaces have been employed in many studies [26–30]. Advances, including resistively heated, gold-coated quartz liners surrounded by a vacuum-insulated outer shell, have pushed the upper limit of transparent furnaces to approximately 1,200 °C [31,32], which is high enough for the growth of some scintillator crystals [33–35]. Nevertheless, transparent furnaces are inherently limited to the growth of compounds with transparent crystal or melt that have a fairly low melting point. The need for a large enough pitch to see between opaque heater coils also severely limits the temperature profiles that may be employed with transparent furnaces.

X-rays have been employed to observe the solidification of higher-melting point compounds, including metals and semiconductors. Chikawa [36] developed a technique for the direct viewing of high-temperature samples via X-ray topographic images over an area of 13 × 9 mm. Using this technique, interfaces of melting and growing silicon crystals in vacuum were observed for samples of 0.8–1 mm thickness. Grange et al. [37] performed *in-situ* imaging of the melting and solidification of a 1 mm-thick aluminum crystal using synchrotron X-ray topography. Barber et al. [38] employed radiography to image a 2 mm-diameter ampoule and contents during the Bridgman growth of germanium (using x-rays) and lead tin telluride (using gamma-rays). Ozawa and Fukuda [39] employed X-rays to carry out *in-situ* observations of the shape of the solid/liquid interface in the melt growth of gallium arsenide. Kakimoto et al. [40] carried similar *in-situ* observations of silicon crystal growth in the Czochralski method and continued to further develop X-ray radiography for the study of these systems [41–48]. Koster and co-workers [49–56] employed real-time X-

ray radiography techniques to measure the solidification in several Bridgman systems. More recently, Pernot et al. [57] designed a small furnace for X-ray transmission diffraction imaging studies capable of attaining temperatures of up to 800 °C to study the growth of small samples, of size 8 × 8 × 0.5 mm. While such prior studies have allowed for direct observations of phase change, they have typically been limited to the study of samples that are orders of magnitude smaller than those produced in bulk crystal growth systems due to the strong absorbance of X-rays by most materials.

Due to their weak interactions with most matter, neutrons are an ideal tool to probe large-size systems that would be opaque to x-rays or electrons, thus enabling non-destructive and *in-situ* studies. In recent, ground-breaking work, Tremsin and co-workers have employed energy-resolved neutron radiography to image the europium concentration field, in real time and *in situ*, during the vertical gradient freeze growth of BaBrCl:Eu [58,59]. These measurements provided a direct observation of segregation and interface shape within a VGF system that is large enough to exhibit the complex interplay of heat transfer, fluid flow, segregation, and phase change characteristic of an industrially relevant melt-growth process.

Here, we describe and apply computational models to analyze the VGF crystal growth system employed in the neutron imaging experiments of Tremsin et al. [58,59]. We discuss the process of building and characterizing the models for this growth system, followed by a detailed examination of factors that influence process behavior. We demonstrate that the model provides a rigorous framework to understand the mechanisms that are responsible for the complicated evolution of interface shape and dopant distribution observed in this VGF growth experiment. Thus, neutron imaging and computational modeling together provide a means to reveal what has heretofore been hidden in Bridgman crystal growth processes.

## 2. Experiments

### 2.1. Methods

Fig. 1 schematically depicts the experimental system, where the VGF furnace, containing the crucible and its charge of BaBrCl:Eu, was placed a few centimeters in front of the detector. Short-pulsed moderated neutrons were directed through the furnace, towards a 28×28 mm² neutron counting detector [60,61] that was installed approximately 8.2 m from the source at Los Alamos National Laboratory. Both the position and time of each detected neutron were measured, with resolutions at the detector of approximately 55 μm and 0.1–1 μs, respectively. Images were acquired for a range of neutron energies, as measured via time-of-flight.

While BaBrCl is opaque to conventional X-rays [62], it does not

interact strongly with neutrons. However, europium attenuates neutrons over a range of energies, thereby providing the possibility for a good contrast image. Thus, the Eu composition is readily determined via the measured image brightness. Due to segregation of the europium between the melt and growing solid, the position and shape of the melt-crystal interface is readily observed in the images.

In preparation for the growth experiment, a charge of BaBrCl was doped with 5 mol % Eu and sealed under vacuum into a quartz ampoule of inner diameter 12.3 mm. The ampoule was then mounted in a modified clamshell furnace, whose single heating zone was monitored by a set-point thermocouple embedded within the insulation surrounding the internal bore. After melting the charge until only a small region of crystalline solid remained in the tip of the ampoule, crystal growth was carried out in a gradient freeze manner by decreasing the furnace set-point temperature at a uniform rate over approximately 13 h.

The technology behind the neutron imaging has been previously explained in Ref. [58], while the original results from the BaBrCl:Eu growth experiment have been presented in Ref. [59]. Subsequent application of energy-resolved neutron imaging techniques have been applied to observe the real-time Bridgman growth of Cs<sub>2</sub>LiLaBr<sub>6</sub>:Ce [63] and to study diffusional processes during phase change [64]. Neutron diffraction has also been applied to measure BaBrCl:Eu structure evolution after crystal growth [65] in order to better understand crystal cracking [66,67].

## 2.2. Imaging of BaBrCl:Eu growth run

Fig. 2(a) shows images that were acquired during the February 2016 VGF growth of BaBrCl:Eu. Much more detailed accounts of the growth experiments have been presented in [58,59]. The upper pictures, Fig. 2(a), show the images obtained during the crystal growth procedure, with the time since the start of growth indicated. Images are integrated over 30 min and acquired for neutrons in the energy range of 9.76 meV – 31.10 meV. Europium attenuation is dominant in our material in this energy range, therefore the contrast observed in this image is primarily due to variation of Eu concentration. The darker contrast corresponds to regions of higher europium concentration.

The image at 1 h shows a small region of newly grown crystal, which is lighter in contrast due to the lower concentration of Eu caused by segregation and a distribution coefficient of less than unity [59]. The

melt is darker, indicating a higher concentration of Eu, and a darkening of contrast is evident above the growth interface in this and subsequent images, which is consistent with the formation of a diffusion layer, enriched with Eu rejected at the interface during growth [68–73]. As time proceeds, the solid/liquid interface moves upwards, indicating the growth of the crystal.

An interesting feature of the Eu distribution in the grown crystal is indicated by the arrow next to the 10-h time image. This arrow points to a band of solid where the local concentration of Eu is noticeably lower, as indicated by the lighter contrast. The growth conditions leading to the formation of this compositional striation are discussed below in Section 4.3.

Fig. 2(b) shows a series of images that have been constructed by taking the ratios between consecutive time frames at various stages during growth. These images show a dark band that arises from the signal difference between newly formed crystal, at lower-concentration, that has solidified from the higher-concentration melt. The resulting signal thus indicates the movement of the solid/liquid interface between frames. Interestingly, the shape of the growth interface clearly changes in time, starting with a shape that is concave with respect to the solid, flattening at approximately 4 h, and finally forming a convex shape during the later stages of growth.

## 3. Computational modeling

We apply several computational modeling approaches to analyze the growth experiments described above. For the sake of brevity, we do not present a detailed discussion of the mathematical approaches nor the numerical methods employed, rather the interested reader is referred to the following references. We describe the development and application of continuum mathematical models and their numerical solution to describe crystal growth processes in Refs. [74–78]. Descriptions of the furnace-level CrysMAS code, developed by the Fraunhofer Institute for Integrated Systems and Device Technology, are presented in [79–83]. The finite element code, Cats2D, used here for detailed computations of heat transfer, phase-change, melt flow, and dopant segregation within the growth ampoule, is detailed in [75,84]. Finally, the strategies employed for the coupled CrysMAS–Cats2D code are presented in a series of papers [85–88]. What follows is a discussion of the rationale and application of these models for subsequent analysis of the growth experiments.

### 3.1. Furnace model and validation

The quantitative description of a melt crystal growth system requires a realistic representation of heat transfer within the growth furnace. Toward this task, we employ the CrysMAS code, which is particularly well suited to compute conductive and radiative heat transport in technologically complex crystal growth furnaces. Fig. 3(a) shows its application to compute the temperature field within the empty (open-bore) clamshell furnace employed for the growth experiments. The temperature distribution is presented on the right, while, on the left, the geometry of the system is depicted, showing how this single-zone furnace was modified by the removal of existing insulation and the insertion of a conical ampoule holder in the bottom of the furnace bore.

The axial temperature profile was measured along the system centerline in the open-bore furnace under several set-point temperatures using a thermocouple probe, and these data are plotted as points in Fig. 3(b). Power input to the furnace zone was controlled by the set-point temperature, measured via a single thermocouple that was embedded within the furnace insulation near the inner bore. Special care was employed for the data corresponding to the 800 °C set-point temperature profile (blue diamonds). In taking these data, we found it was very important to move the thermocouple, measure the temperature over time, and then ensure that the thermocouple had reached a steady-

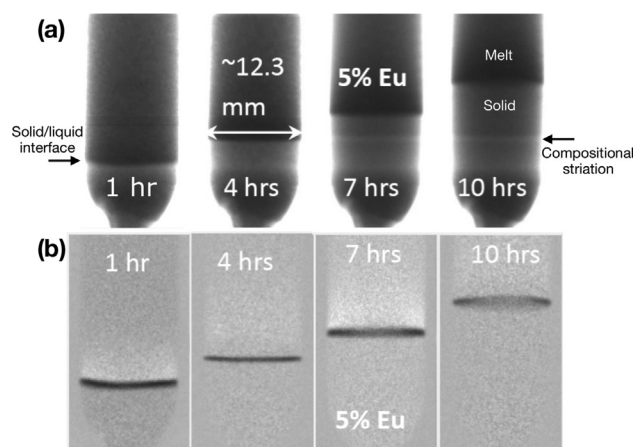


**Fig. 2.** (a) Neutron transmission contrast images of the BaBrCl:5%Eu sample during the crystal growth experiment. Darker contrast corresponds to higher Eu concentration. The time since the start of crystal growth is indicated in each image. (b) The ratio of two consecutive images is shown to emphasize the location of the solid/liquid interface. The dark band corresponds to the distance over which the interface has moved between successive images and is caused by the discontinuous jump in europium concentration across the interface caused by segregation. Images adapted from [59].

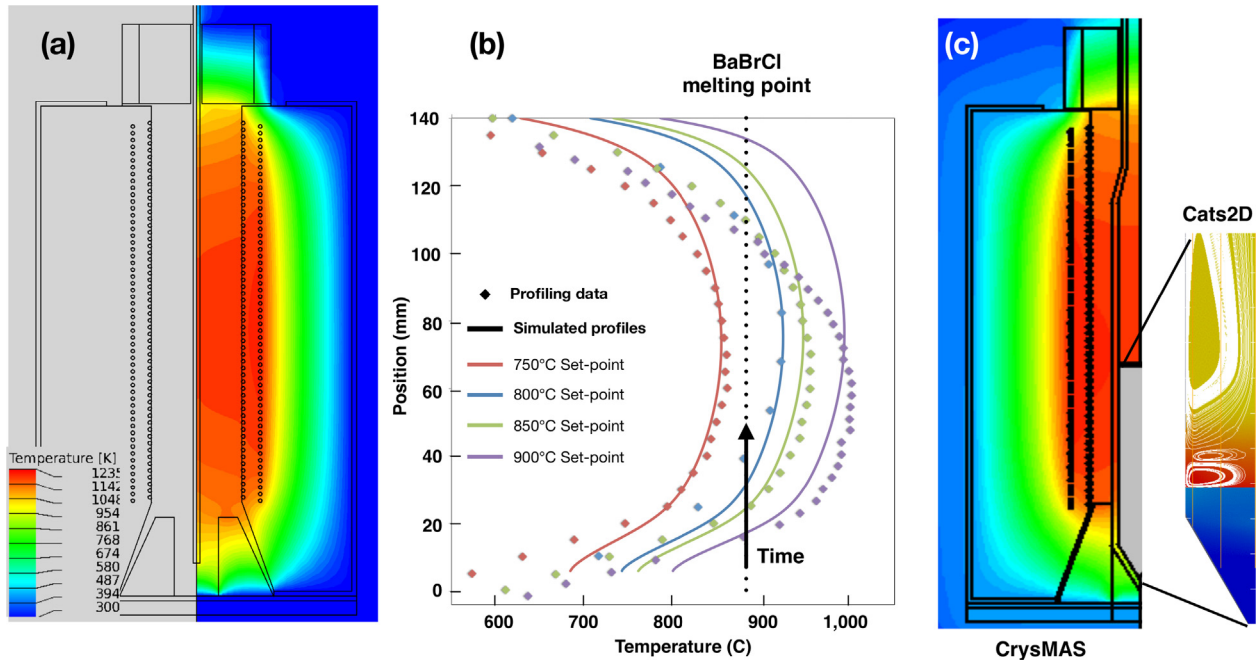


**Fig. 3.** (a) CrysMAS computational model for the modified clamshell furnace used for the crystal growth experiments that depicts the single zone of heating elements wound about the bore and the modified bottom, with conical ampoule holder. The image on the right shows a predicted thermal field for the open-bore furnace. (b) Measured points and predicted curves of the axial thermal profiles for the open-bore furnace at various set-points. Vertical gradient freeze growth is accomplished by reducing the set-point temperature over time, thus moving the melting point upward and driving crystal growth. (c) A depiction of the fully coupled CrysMAS–Cats2D model that is used to compute segregation during growth. The colors plotted for the furnace on the left depict temperature: the ampoule image on the right depict Eu concentration by color and pathlines for the melt flow in white.

state after moving it.

CrysMAS predictions of the thermocouple temperatures are shown by the solid curves in Fig. 3(b). The predicted temperatures in the upper portion of the furnace are higher than measured. This was likely due to the effects of convective cooling through the open bore in the actual furnace, an effect that was not modeled in CrysMAS and that lead to overly high temperature predictions. Notwithstanding, the agreement between the predicted profile and measurements is quite good in the bottom region of the furnace. In addition, the agreement between CrysMAS predictions and the 800 °C set-point temperature profile is notably better than for the 850 °C and 900 °C set-points, likely due to the extra effort in its measurement, as described above.

These computations were performed using reported physical properties for all of the furnace elements, and no adjustable parameters were used to improve the match between model and experiment. We deemed that the correspondence between model and measurements was good enough to validate the model for further studies of growth, particularly since the profiles over the lower regions of the furnace, where the ampoule was placed during the growth experiment, agreed quite well for all furnace set-points.

The melting temperature of BaBrCl, approximately 895 °C, is indicated in Fig. 3(b), along with a depiction of the progression of the temperature profiles in the furnace with time. In the vertical gradient freeze approach applied here, the furnace set-point is progressively decreased in time, moving the melting temperature upward in the furnace. This drives the solid/liquid interface upward, resulting in growth.

### 3.2. Crystal growth models

In the previous section, we discussed the use of CrysMAS to model furnace-scale heat transfer. The next step of modeling the actual crystal growth process requires a careful consideration of what issues are of interest. For this VGF system, the length scales are small and the thermal gradients are low, so we expect the flow in the melt will be

relatively weak. Whether it is weak enough to ignore in a crystal growth model requires some scaling analysis [72,77,78] and preliminary calculations. We therefore aim to estimate the magnitude of buoyancy-driven flows in the melt of this system.

Critical to this calculation is an estimate of the radial temperature difference  $\Delta T$ , leading to a density difference  $\rho\beta\Delta T$  upon which gravitational acceleration  $g$  acts over the lever-arm distance of  $R$  to drive flow. Here,  $\rho$  is the density of the melt,  $\beta$  is its thermal expansion coefficient, and  $R$  is the inner ampoule radius. We estimate  $\Delta T$  from the axial thermal gradient and the observed deflection of the isothermal solid/liquid interface in this system. A characteristic interface deflection is observed as  $0.06 \times R = 0.37$  mm, see the data presented in Fig. 4(d) which is multiplied by an axial gradient of 2 K/mm (estimated from measurements presented in [59]) to give  $\Delta T \approx 0.74$  K.

Under this radial temperature difference and using the estimated physical properties of BaBrCl from Table 1, the dimensionless Grashof number, a measure of the buoyancy driving force [78], is given as,

$$Gr = \frac{g\rho^2\beta\Delta TR^3}{\mu^2} \approx 350, \quad (1)$$

where  $\mu$  is the viscosity of the melt.

With such a small value for  $Gr$ , we expect the melt flow to be relatively weak. For such flows, we do not expect inertia to be significant, so a dominant balance suggests that the velocity should scale linearly with the buoyant driving force [78]. An upper limit for such a velocity would be represented by the expression for well-developed flow in a differentially heated vertical channel [89], which predicts a maximum velocity of

$$v_{max} = \frac{g\beta R^2 \Delta T}{73\sqrt{3}\nu} \approx 0.47 \text{ mm/s}, \quad (2)$$

when applied to a cylindrical geometry representing the growth ampoule.

However, even this estimate is much larger than what is computed for this system. From the coupled model calculations performed here



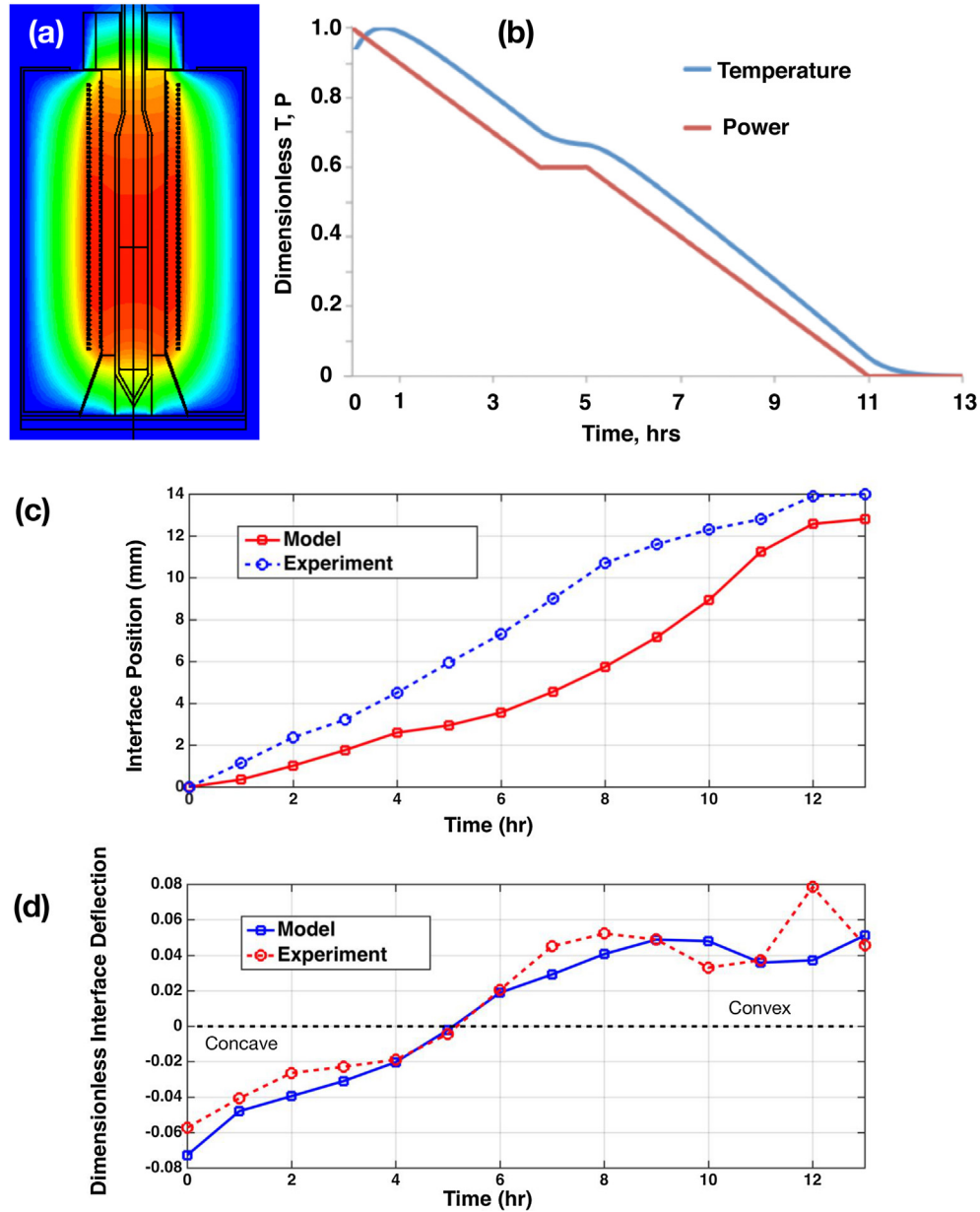


**Fig. 4.** (a) The predicted temperature field in the furnace and ampoule is shown at start of growth. The color scale is the same as presented in Fig. 3(a). (b) The input power to the model and the predicted temperature measured at the set-point location are plotted as functions of growth time. (c) The position of the solid/liquid interface, measured from its initial axial position, is plotted as a function of growth time for model and experiment. (d) The dimensionless deflection of the solid/liquid interface, defined as  $(H_0 - H_R)/R$ , is plotted as a function of growth time for model and experiment.

and finite-element computations of the Bridgman growth of BaBrCl under an axial gradient of 20 K/cm (2 k/mm) [67], we find that  $v_{max} \approx 0.035$  mm/s. This much smaller velocity, compared to the estimate provided by Eq. (2), is likely due to the thermally stabilizing configuration of this vertical system, with cooler, denser melt underlying warmer.

Using the computational results of  $v_{max} \approx 0.035$  mm/s, we finally estimate a Reynolds number of  $Re = \rho_\ell v_{max} R / \mu \approx 0.21$ . Since  $Re$  is a measure of inertial to viscous effects in the flow, a value of  $Re < 1$  confirms our assertion that inertia is not important for the flow in this system.

Furthermore, we assess the importance of melt flow and convective heat transfer in the melt via the thermal Peclet number,  $Pe_h = v_{max} R / \alpha_\ell$ , and the importance of convective solute transport in the melt via the solutal Peclet number,  $Pe_s = v_{max} R / \mathcal{D}_\ell$ ; see, e.g., [72,77,78]. In these expressions, the melt thermal diffusivity is  $\alpha_\ell = k_\ell / \rho_\ell C_{p,\ell}$ , with  $k_\ell$

denoting the thermal conductivity,  $\rho_\ell$  the density, and  $C_{p,\ell}$  the heat capacity, and  $\mathcal{D}_\ell$  is the diffusivity of europium in the melt. Using the estimated properties of BaBrCl from Table 1, we calculate  $Pe_h \approx 0.56$ . The thermal Peclet number represents a measure of the ratio of convective to conductive heat transfer in a fluid. For  $Pe_h < 1$ , we argue that heat transfer by melt convection is less important than conduction in the VGF system considered here. On the other hand, the solutal Peclet number, which provides an estimate of the importance of convective to diffusive transport of a species in the melt, is estimated as  $Pe_s \approx 22$ . Clearly,  $Pe_s \gg 1$ , and we must account for fluid dynamics to accurately describe solute transport in the melt and its effects on segregation of Eu.

Based on these arguments, we choose to apply CrysMAS, which accounts for heat transfer via conduction and radiation but neglects convection in the melt, to predict the changing thermal field with time. These calculations of the overall dynamics of growth in this system are presented in Sections 4.1 and 4.2.

**Table 1**  
Physical properties of BaBrCl:Eu used in the simulations.

|  |              |                    |                                  |
|--|--------------|--------------------|----------------------------------|
| Thermal conductivity (W/m K)                     | Solid        | $k_s$              | 1.1 [93]                         |
| Heat capacity (J/kg K)                           | Liquid       | $k_\ell$           | 0.7 [Estimated]                  |
|  | Solid        | $C_{p,s}$          | 423 [96]                         |
|  | Liquid       | $C_{p,\ell}$       | 423 [Estimated]                  |
| Density (kg/m <sup>3</sup> )                     | Solid        | $\rho_s$           | 4320 [90]                        |
|  | Liquid       | $\rho_\ell$        | 4320 [Estimated]                 |
| Viscosity (kg/m s)                               | Liquid       | $\mu$              | $4.5 \times 10^{-3}$ [94]        |
| Eu Diffusion coefficient (m <sup>2</sup> /s)     | Solid        | $\mathcal{D}_s$    | 0 [Estimated]                    |
|  | Liquid       | $\mathcal{D}_\ell$ | $1.0 \times 10^{-8}$ [Estimated] |
| Thermal expansion coefficient (K <sup>-1</sup> ) | Liquid       | $\beta$            | $2.23 \times 10^{-4}$ [95]       |
| Eu Segregation coefficient                       | Solid-liquid | $k$                | 0.5 [59]                         |
| Latent Heat of fusion (J/kg K)                   | Solid-liquid | $\Delta H_f$       | 96,000 [92]                      |
| Melting Point (K)                                | Solid-liquid | $T_m$              | 1,168 [91]                       |

Also from these arguments, the analysis of europium transport and segregation during growth requires a detailed accounting for melt flows. For this task, we apply a more complicated modeling approach that couples the furnace heat transfer calculations of CrysMAS with a finite-element code, Cats2D [84], which computes heat transfer, melt convection, solidification, and segregation occurring within the ampoule [75]. As in our prior coupled models [85–88], we apply CrysMAS to compute global heat transfer within the furnace, with an excluded, inner domain comprising the contents of the ampoule. Cats2D is then applied to model crystal growth within the ampoule, accounting for heat transfer, phase change, melt flow, and dopant transport and segregation. Self-consistent boundary conditions are applied along the coupling boundary (the inner ampoule wall) to enforce continuity of the temperature field and heat fluxes. A depiction of the two codes and their respective domains is presented in Fig. 3(c).

Transient calculations were performed using these two codes via implicit time integration with a fully coupled, approximate block Newton (ABN) iterative method, as described in [87,88]. The coupled CrysMAS–Cats2D model is applied to understand Eu segregation during growth in this VGF system in Section 4.3 below.

### 3.3. Physical properties of BaBrCl:Eu

While the physical properties of the components comprising the clamshell furnace were known *a priori*, the properties of BaBrCl were not, other than its melting point and density [90,62,91]. We therefore estimated the properties of solid and molten BaBrCl, guided by values measured for other mixed-halide salts and crystals [92–96]. We then performed a series transient simulations to compare predicted and measured values of interface position and shape using different values for unknown properties [66]. The resulting estimates for physical properties used in the BaBrCl growth simulations conducted here are listed in Table 1. Updated values for some of these properties, obtained via more recent measurements of the BaBrCl:Eu system at Lawrence Berkeley National Laboratory, are reported in [66,67].

## 4. Results and discussion

### 4.1. Global behavior

Fig. 4(a) shows the temperature field in the crystal growth system near the start of growth, as computed by CrysMAS. The crystal growth process is simulated by time-dependent changes in the power input to the heating coils of the single-zone furnace. Following the same time schedule as used in the experiment, input power is ramped up to achieve temperatures high enough to melt most of the charge, followed

by a hold period of approximately one hour. After the hold, growth commences at  $t = 0$  via a time-dependent reduction in power to the zone of the furnace, as depicted by the red lines in Fig. 4(b). The initial power level is chosen to match the upper set-point temperature of the experiment, and the power ramp rate is chosen to reproduce the temperature ramp rate of the experiment. The predicted temperature at the set-point location in the furnace is shown by the blue curve in Fig. 4(b). Both power and temperature are represented in dimensionless terms as  $P = (\tilde{P} - \tilde{P}_{min})/(\tilde{P}_{max} - \tilde{P}_{min})$  and  $T = (\tilde{T} - \tilde{T}_{min})/(\tilde{T}_{max} - \tilde{T}_{min})$ , respectively, where the tilde represents the dimensional value of each variable.

Note that there are some uncertainties associated with both experiment and simulation with regard to these profiles. First, the CrysMAS calculations of the furnace set-point temperature, shown by the blue curve in Fig. 4(b), indicate a rise and fall over the first hour or so after the power ramp-down is begun at  $t = 0$ . This indicates that the hold period before growth was likely not long enough to allow the growth system to thermally stabilize to a stationary state. This predicted transient in the temperature field also makes it unclear if our designated  $t = 0$  actually marks the start of growth.

Finally, the power input to the simulation is also meant to represent an unanticipated event that occurred during the experiment. After the initiation of growth and unbeknownst to the experimental team, the controller locked up at a constant set-point temperature for approximately one hour. This event is represented by a one-hour pause in the power reduction schedule, where the input power was kept constant between hours 4 and 5. While this power input plateau is meant to model the controller lock-up event, the precise timing of the actual event is not known.

The position of the solid/liquid interface at the center of the ampoule is plotted as a function of growth time in Fig. 4(c), using data from the imaging experiments and model predictions. A description of the processing techniques employed to extract interface location and shape from the contrast images is presented in Appendix A. The slope of the experimental curve indicates that the growth rate is fairly uniform, at  $V_g \approx 1.5$  mm/hr, over the first 8 h. From 8–12 h, growth slows to approximately  $V_g \approx 0.8$  mm/hr. Comparison of the two curves shows that the model initially predicts a slower progression of the interface, compared to that measured in the experiment. However, a shift of the model curve to the left, to represent the possible start of growth at a later time than our identified  $t = 0$ , would bring the early-time behavior in better agreement. There is also a mismatch between model and experiment over the time period when the controller locked up. As discussed above, this mismatch may partially be related to our assumptions about the timing and duration of the actual event.

The trends in growth velocity qualitatively agree between model and experiment, as shown by the slope of the curves of Fig. 4(c). Namely, a substantial period of nearly constant growth rate occurs at the start of the growth run (0–6 h for the experiment), followed by an increase in growth rate (6–8 h for the experiment), and ending with a slowing of growth (8 h and onward for the experiment). However, there are disagreements between the quantitative measures and predictions of growth rate values.

In particular, during the first 8 h of growth, the CrysMAS model predicts an average growth velocity of  $V_g \approx 0.73$  mm/hr, roughly half that observed in the experiment. We believe that the underprediction of growth rate is due to the neglect of melt convective heat transfer in our CrysMAS model. Recall that our estimate of the Peclet number for heat transfer was  $Pe_\ell \approx 0.56$ . While this number is small enough to argue that radial heat flows are dominated by conduction, the axial heat flows through the melt would be expected to be more strongly affected by convection. With a larger role of convective heat transfer through the melt, the system more quickly follows the changing set-point temperatures, thereby supporting faster growth rates in this VGF system. While convection in the melt could be included in the CrysMAS computations to check these assertions, the very significant, additional

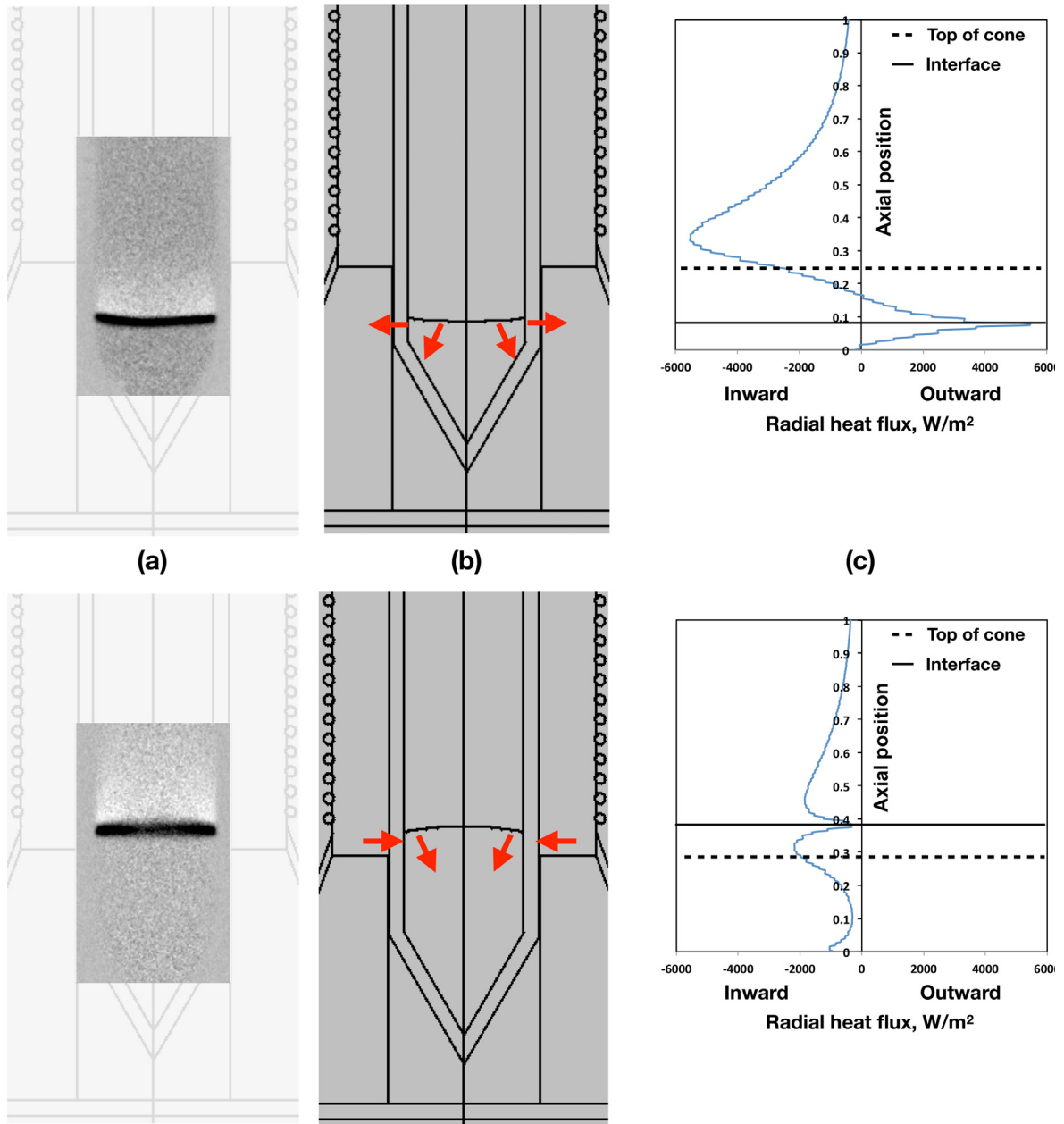


**Fig. 5.** Top images: Concave interfaces are observed during early stages of growth. Bottom images: Convex interfaces arise during later stages of growth. (a) Contrast image showing the shape of the interface observed in experiment. (b) The model prediction of the interface shape is plotted over the system geometry, with red arrows indicating the direction of heat flows near the interface. (c) The radial heat flux along the inner ampoule wall computed by the model is plotted with axial position. Horizontal lines indicate the axial positions of the top of the seed-holder cone (dotted) and the solid/liquid interface (solid).

effort in set up and in computation was not deemed worthwhile, particularly in light of the good agreement in predictions of interface shape that are discussed below.

The shape of the solid/liquid interface, represented via a dimensionless deflection defined at  $(H_0 - H_R)/R$ , where  $H_0$  is interface height at the centerline and  $H_R$  is height at the ampoule wall, is plotted as a function of growth time in Fig. 4(d). As is apparent from the contrast images presented in Fig. 2(b), the interface deflection shown in Fig. 4(d) evolves from negative to positive, indicating a transition from a concave interface to convex. The predicted interface deflection agrees very well with experiment. We posit that the outlier value for interface deflection in the experiment at 12 h was caused by noise in our interface extraction procedure (see Appendix A). We examine the physical mechanisms responsible for the change in interface shape in the following section.

#### 4.2. Interface shape and heat transfer

Figs. 5 shows a comparison of interface shapes at two different stages of growth. The upper images show a concave interface that is present during the early stages of growth, which is evident in the frame contrast picture of upper image (a). Image (b) shows the shape and position of the interface predicted by the model at the same stage of growth. The direction of heat flows near the interface are indicated by the red arrows in image (b). Since the solid/liquid interface lies along the melting-point isotherm, heat must flow in a direction normal to it [77,97,98]. Here, the radial component of the fluxes near the interface is directed outward. This is consistent with the radial heat flux along the inner ampoule wall computed by the model, depicted in the right image (c), which shows that heat is flowing radially outward near the interface.

The lower images show a later stage of growth, where the interface shape has become convex. Image (a) shows a frame contrast picture from the neutron imaging in which the convex solid/liquid interface is evident. The model prediction of this interface shape, shown in lower image (b), again agrees very well with experimental observation. The convex interface is accompanied by different heat flows compared to the concave shape. Along the convex interface, the radial component of heat flux is inward. The lower image (c) shows that the computed radial heat flux along the ampoule is negative, directed inward, for this stage of growth.

From these model results, we can surmise the origin of the change in interface shape. Heat is always flowing axially during growth, from the hotter melt above to the cooler crystal below. In this system, the ampoule containing the BaBrCl charge is mounted in a conical holder at the bottom of the heating zone. This design promotes heat loss from the bottom of the furnace, setting up the axial temperature gradient needed to establish the crystal phase below and the melt above.

However, the radial heat flows change significantly with axial position in this vertical gradient freeze furnace. Traveling up from the bottom of the system, the ampoule contained within the conical holder is first surrounded by the cooler, refractory ceramic of the holder. Continuing above the top of the conical holder is the inner bore of the furnace, which is wrapped with active heating elements. As the solid/liquid interface moves from within the conical ampoule holder to within the furnace bore, the radial flow of heat changes from outward to inward. Accordingly, the top of the ampoule holder cone marks the transition from a concave to convex growth interface.

#### 4.3. Eu segregation and fluid dynamics

Of particular interest in this VGF experiment is the distribution of europium in the grown crystal. Examination of the neutron transmission contrast images presented in Fig. 2(a) clearly show the segregation of Eu between the melt (darker regions) and the crystal (lighter regions). To understand these effects, we apply the coupled CrysMAS—Cats2D model to perform detailed computations of Eu solute transport and segregation.

This transient simulation was performed using the coupled model with the same thermal inputs as described in Section 4.1 and with the additional properties, listed in Table 1, needed to compute melt fluid dynamics and solute transport. We assumed that growth was initiated from a steady-state, no-growth condition, with a small amount of solid in the conical region of the ampoule. The initial Eu concentration in the solid was assumed constant at 2.5% and equilibrated with the overlying melt, which was assumed to be at a uniform Eu concentration of 5%. The distribution coefficient for europium was estimated as  $k = 0.5$  from initial growth results [58,59]. In the following computational results, we report nondimensional concentrations, scaled as  $c/c_0$ , where  $c_0$  is the initial melt concentration. The axial and radial positions are also scaled with the ampoule radius, giving dimensionless values of  $r = \tilde{r}/R$  and  $z = \tilde{z}/R$ , where  $\tilde{r}$  and  $\tilde{z}$  are the dimensional distances. The origin of the coordinate system is set at the bottom centerline of the ampoule, and the initial position of the solid/liquid interface is assumed to be located at  $z \approx 1$ .

Fig. 6 shows a series of simulation states captured at discrete interface positions,  $z_i$ , as growth proceeds in time. In each image, a meridional plane, representing the contents of the ampoule, is shown for this axisymmetric system, with the right vertical boundary corresponding to the centerline of the ampoule. The Eu composition is shown in both the solid and liquid phases via the indicated color scale. The solid/liquid interface is clearly represented by the different colors corresponding to the discontinuity in Eu concentration between the two phases. The solid is blue for lower concentrations of Eu, and the melt has Eu dimensionless concentrations of  $c/c_0 \geq 1$ , which increase over time due to the rejection of Eu at the growth interface.

Pathlines, computed by integrating the motion of massless tracer

particles in these transient flows, are plotted for the states of Fig. 6, and shown by the white curves in the melt region. These curves illustrate the structure of flows in the melt, and the spacing between them indicates the magnitude of the flows. Their spacing is inversely related to local flow magnitude—more closely spaced tracer lines indicate stronger flows. The local velocity field is everywhere tangent to these pathlines, and the direction of flow is given by the sense of circulation of vortices comprised of closed tracer paths. A positive marker at the center of a flow vortex indicates counterclockwise circulation, while a negative marker means that the vortex is flowing in a clockwise sense.

Understanding the subsequent effects of the flow field on Eu segregation will be discussed by referring to the compositional fields for each state depicted in the images of Fig. 6 along with their corresponding axial concentration profiles in Fig. 7. Each plot in Fig. 7 shows the dimensionless Eu concentration plotted axially at three different radial positions, as noted by the legend in the plot corresponding to  $z_1$ . Simulation results are organized in several sections below to facilitate the discussion of phenomena of interest, with a final section presenting a comparison of the predicted and measured Eu centerline profiles.

##### 4.3.1. Initial transient

The initial state of the system, corresponding to an interface height of  $z_0$ , is shown in Figs. 6 and 7. The initial compositions are constant in the solid and melt at  $c/c_0 = 0.5$  and  $c/c_0 = 1.0$ , respectively. Fig. 6 shows the stationary interface to be very slightly concave, with uniform Eu compositions in each phase. Interestingly, there is a very complicated flow structure throughout the melt. High in the ampoule, the outer melt near the ampoule wall is hotter and less dense than that in the interior, and buoyancy drives a strong, clockwise vortex, with liquid flowing upward along the ampoule wall and downward along the centerline. A series of alternately rotating vortices are encountered traveling downward toward the solid/liquid interface. The counterclockwise vortex near the centerline is very weak; its existence is inferred by the outward deflection of the downward flowing fluid from the larger, upper vortex. A separated lobe of the upper vortex is nested near the corner junction of the ampoule (where the conical portion joins with the cylindrical region). Below this point, the radial heat flows reverse to outward (see the lower case in Fig. 5c), so that the interior melt temperature is higher than that near the ampoule wall. This drives a reasonably strong, counterclockwise vortex that streams fluid inward across the interface and upward along the centerline. Note that even though this flow structure is spatially complicated, the flows, with a Reynolds number of  $Re = 0.21$  (estimated in Section 3.2), are laminar and dominated by viscous effects.

The state shown by  $z_1$  in Fig. 6 shows the system after approximately 1 h of growth, with the interface reaching a dimensionless position of  $z \approx 1.5$ . The structure of the melt flow is quite similar to that the initial state, with the same four, axially stacked vortices; however, the bottom two have shrunk in size as the growth interface has moved upwards. Europium rejected by the growing crystal has resulted in an enriched region of Eu concentration above the interface. This is also shown by the axial profiles at time  $z_1$  in Fig. 7. The axial Eu concentration in the melt shows a maximum at the solid/liquid interface and decreases toward the bulk of the melt, where  $c/c_0 \rightarrow 1$ .

The formation of the enriched Eu diffusion layer is consistent with classical theories of axial segregation [68,70]. However, the diffusion layer is not as extended as would be expected under steady-state conditions, where its characteristic length, in dimensionless terms, would be  $\frac{D_E}{R} \approx 3.9$ , with the solidification growth velocity of  $V_g = 1.5$  mm/hr (estimated in Section 4.1 by the slope of interface position versus time in Fig. 4c). Instead, the diffusion layer exists from the interface at  $z \approx 1.5$  to  $z \approx 3$ , covering a distance of less than half the expected characteristic length. This difference is explained by the flows in the melt. Near the interface, the flows are weak enough to allow the



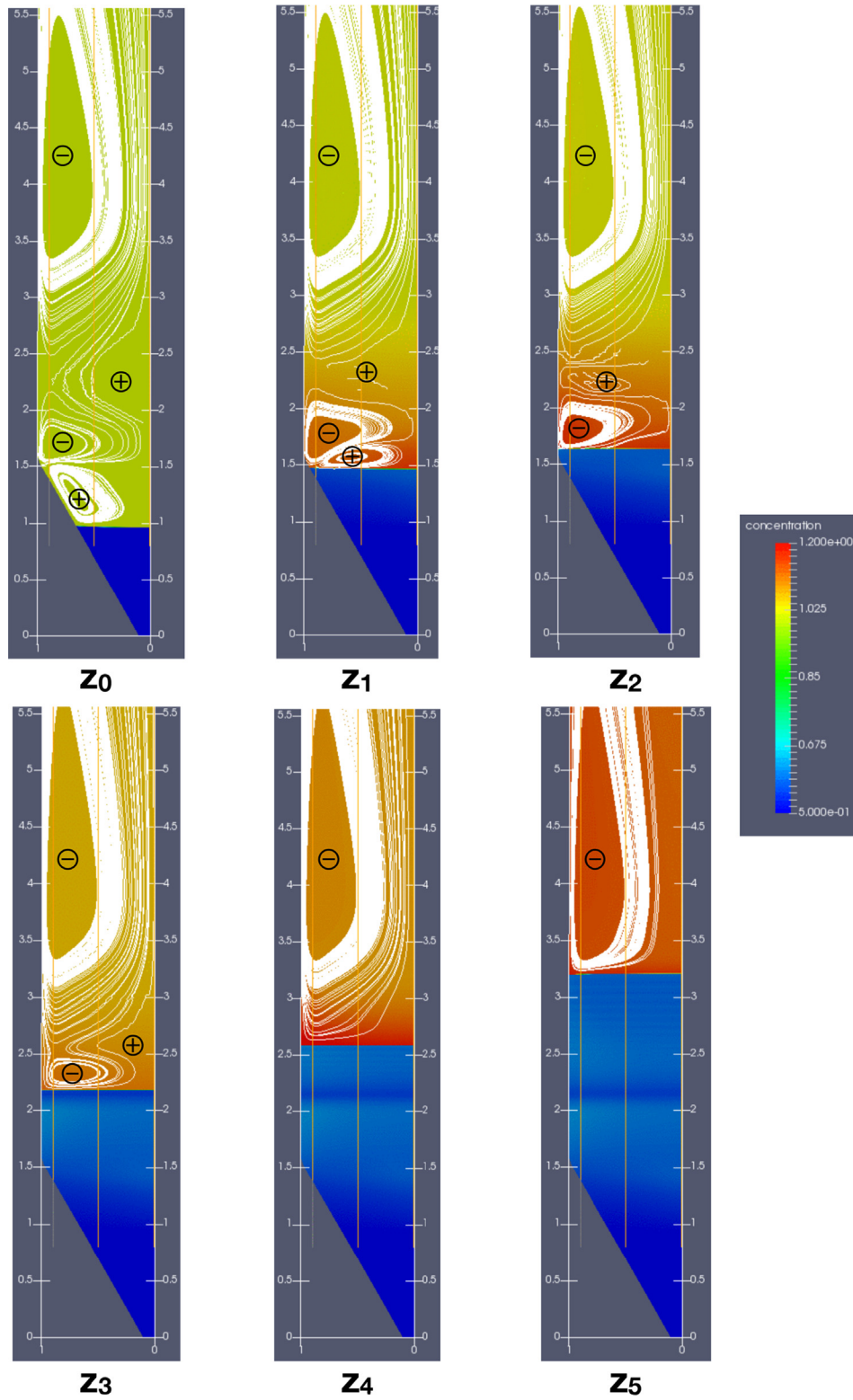


**Fig. 6.** Europium composition fields and melt pathlines are shown for the coupled, CrysMAS–Cats2D model at selected stages of growth, identified as  $z_i$ , the nominal interface axial position. A positive marker at the center of a flow vortex indicates counterclockwise circulation; a negative marker shows clockwise flow. The color scale on right represents dimensionless europium (Eu) concentration,  $c/c_0$ . Axial Eu concentration profiles for the corresponding growth stages,  $z_i$ , are shown in Fig. 7. (For interpretation of the references to colour in this figure legend, the reader is referred to the web version of this article.)

rejected Eu to form an axial diffusion layer; however, the strong, upper vortex convectively mixes the solute and produces a constant concentration. The lower extent of this strong vortex is seen in Fig. 6 to lie at  $z \approx 3$ , which marks the end of the diffusion layer shown in Fig. 7.

The detailed shapes of the concentration profiles though the diffusion layers shown for  $z_1$  in Fig. 7 are influenced by the weak flow cells near the solid/liquid interface. First, notice that, in both solid and melt, the axial profile near the centerline (red curve,  $r = 0.01$ ) is above the

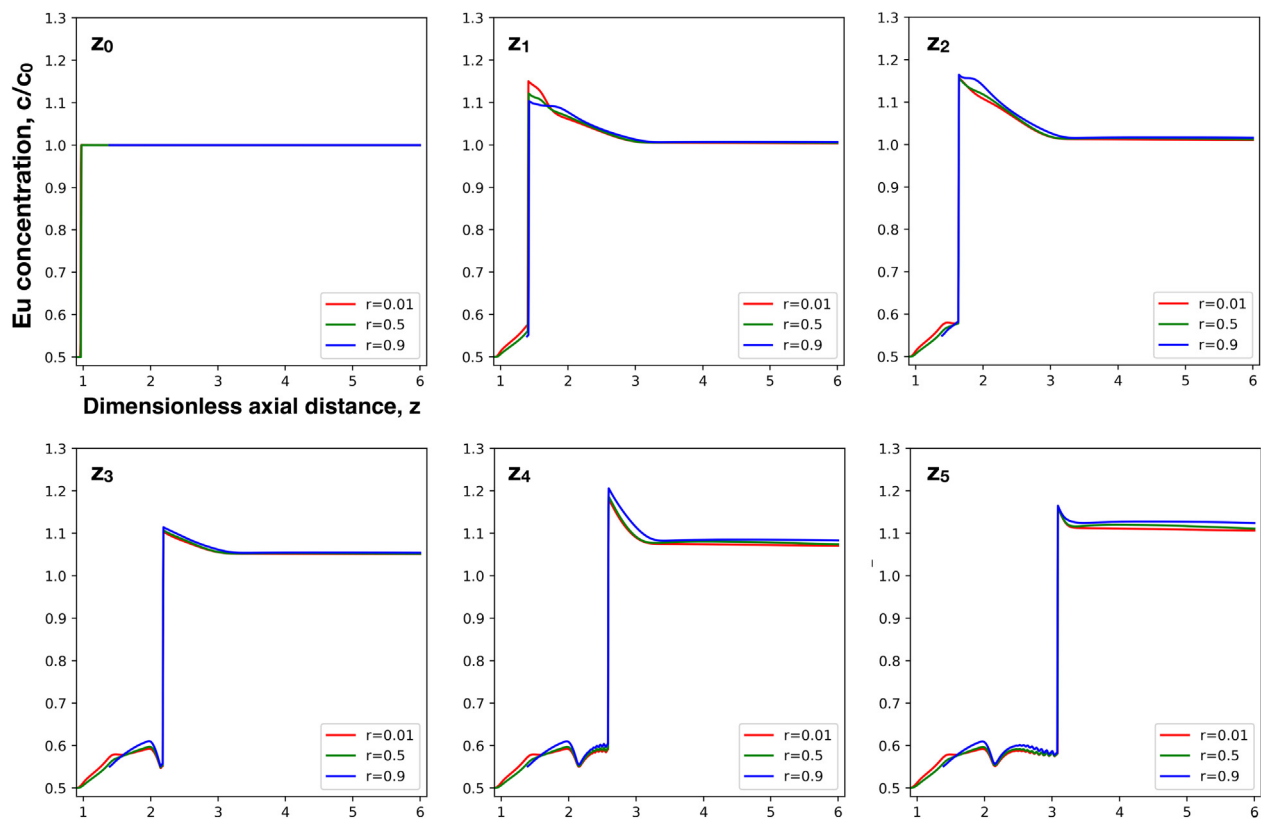


**Fig. 7.** The dimensionless europium (Eu) concentration predicted by the coupled, CrysMAS–Cats2D model is plotted as a function of dimensionless axial distance along different radial positions, as indicated by the legends. The profiles correspond to the growth stages,  $z_i$ , that are shown in Fig. 6.

outer profiles, indicating a radial variation of Eu concentration with higher concentration in the center. This is consistent with the counterclockwise flow vortex that sits just above the growth interface, which sweeps fluid inward (see the positively signed, lower vortex in image  $z_1$  of Fig. 6). Second, the effects of convective mixing are evident in the shape of the axial profiles. Near the centerline (red curve,  $r = 0.01$ ) there is a change in slope at  $z \approx 1.7$  that corresponds with the shear layer separating the lower, counterclockwise vortex and the clockwise vortex above it. Also apparent is a local plateau in axial Eu concentration near the ampoule wall (blue curve,  $r = 0.9$ ) that arises due to mixing caused by the relatively strong, clockwise vortex immediately above the outer portion of the interface. Radial segregation due to melt flows is not described in classical theories of segregation [68–70,99]; however, such effects have been extensively studied more modern approaches that explicitly account for melt convection [72,78,100–104].

At a later time, the growth interface at  $z_2$  has advanced a short distance from the prior state at  $z_1$ ; however, there is a significant change in flow and segregation. As indicated by the pathlines in Fig. 6 at  $z_2$ , the counterclockwise vortex that had been immediately adjacent to the solid/liquid interface has shrunk and nearly disappeared. Simultaneously, the negatively signed vortex, nested in the outer corner of the ampoule, has increased in both size and strength. These changes are caused by the reversal in radial heat flow in the system above the top of the conical ampoule holder, as was discussed in Section 4.2. With the inward-directed radial heat flux, the outer portion of the melt is now warmer than along the centerline. As the outer, clockwise vortex gains in strength, fluid now sweeps rejected Eu from inward to outward along the interface, thus reversing its radial distribution in the melt. This is confirmed by the arrangement of axial concentration profiles at  $z_2$  in Fig. 7, where the outer profile (blue curve,  $r = 0.9$ ) now lies above the other profiles.

#### 4.3.2. Growth pause and compositional striation

The growth stage at  $z_3$  corresponds to the end of the one-hour controller lock-up event. During the lock-up period, the input power to the coupled model is held constant to simulate the actual input to the furnace in the experiment. Since the VGF process relies on a constant rate of powering down to drive growth, the constant power during lock-up causes interface growth velocity to drop to nearly zero. With slowed growth comes a decrease in the rate of Eu rejected and a diminishing concentration at the interface. The reduction in local Eu concentration in the melt is apparent by the change in color between states  $z_2$  and  $z_3$  in Fig. 6. In addition, with the slowing of growth, less latent heat is generated at the phase-change interface, thus reducing the radial temperature gradients and weakening the flows near the interface. This is seen for state  $z_3$  in Fig. 6 by the fewer number of pathlines in the vortices above the solidification front.

The growth slowdown and subsequent rearrangement of the diffusion layer in the melt causes a decrease in the Eu concentration in the melt at the interface, which results in a band of lower-concentration solid. This phenomenon was first explained by Tiller et al. [68] and is known as a compositional striation. Such striations will always occur when there is a time-dependent change in interface velocity during directional solidification. The compositional striation induced by the growth pause is quite apparent in the axial Eu profiles for  $z_3$  and onward shown in Fig. 7 and in the neutron contrast images shown in Fig. 2(a).

#### 4.3.3. Non-classical axial segregation

After the one-hour hold, the decreasing power ramp is reinstated, and growth re-commences with the interface moving upward. By the time that the system reaches state  $z_4$ , the diffusion layer has re-formed in front of the advancing interface, as seen in Fig. 7. However, there is a significant rearrangement of flows between states  $z_3$  and  $z_4$ , as seen in Fig. 6. In particular, the multiple vortices that were stacked above the

interface in state  $z_3$  have disappeared and been replaced by a single vortex that is rotating clockwise in state  $z_4$ . This flow structure persists through the duration of the growth, as seen at  $z_5$  in Fig. 6.

The change in flow structure is very important for setting the length of the diffusion layer, which has significantly shortened between states  $z_4$  and  $z_5$  in Fig. 7. For each of these states, the concentration approaches the constant value of the well-mixed bulk at an axial distance of  $z \approx 3.4$ . This is consistent with the pathlines of states  $z_4$  and  $z_5$  of Fig. 6, both showing that the upper, clockwise vortex remains fixed in space even as the growth interface moves upward.

Classical theories of axial segregation, notably those by Scheil [99], Smith, Tiller and Rutter [70], and Burton, Prim, and Schlichter [69], assume unchanging conditions over the entire growth run, and all predict monotonically increasing solute concentration in the grown solid, when its distribution coefficient is less than unity, as is the case for Eu in this system. However, in the VGF system considered here, time-dependent changes of flow structure cause the size of the diffusion layer to continually decrease from state  $z_4$  to  $z_5$ . This steadily shrinking diffusion layer results in a non-classical, decreasing axial Eu concentration profile in the solid over a significant portion of growth.

This non-classical behavior can be explained via a more flexible interpretation of the segregation theory of Burton, Prim, and Schlichter (BPS) [69]. Indeed, the BPS model predicts that a shorter diffusion layer will decrease the Eu concentration in the growing solid. This model posits a stagnant film of thickness  $\delta$  to exist in front of the interface, and solute transport is assumed to occur only by diffusion within the film and by perfect convective mixing beyond the film. Then, the concentration in the growing solid is given by  $c_s = k_{\text{eff}} c_{\ell, \infty}$ , where  $k_{\text{eff}}$  is an “effective” distribution coefficient and  $c_{\ell, \infty}$  is the concentration of solute in the well-mixed bulk of the melt, far away from the growth interface. The BPS effective distribution coefficient is given by

$$k_{\text{eff}} = \frac{k}{k + (1 - k)\exp(-V_g \delta / \mathcal{D}_\ell)}, \quad (3)$$

where  $k$  is the equilibrium distribution coefficient,  $V_g$  is the growth velocity of the crystal, and  $\mathcal{D}_\ell$  is the diffusion coefficient of the solute in the melt.

The original assumption of BPS was that the thickness of the diffusion layer was constant throughout growth. Clearly, however, its size is changing due to the evolving flow structure in this VGF system. The diffusion layer for each state is estimated from the axial concentration profiles as  $\delta_4 \approx 4.3$  mm and  $\delta_5 \approx 1.2$  mm for states  $z_4$  and  $z_5$  shown in Fig. 7. Presuming that the bulk melt concentration,  $c_{\ell, \infty}$ , does not significantly change between these two states, we can apply the BPS expression, given in Eq. (3) above, to estimate the ratio in the solid Eu concentrations at the interface between the states of  $z_4$  and  $z_5$  to be  $c_5/c_4 \approx k_{\text{eff},5}/k_{\text{eff},4} = 0.96$ . This is very near to the predicted decrease in solid Eu concentration between these states of  $c_5/c_4 \approx 0.58/0.60 = 0.97$ .

Finally, note that the Eu concentration profile for stage  $z_5$  in Fig. 7 exhibits small-amplitude oscillations in the profile through the solid. These oscillations are the result of discretization error that arises from the increasing strength of flow in the melt. As discussed above, a single, counterclockwise vortex arises and strengthens after the growth pause. The effect of the stronger flow is seen by comparing the width of the diffusion layer between stages  $z_4$  and  $z_5$ . As the flow strength increases, the hydrodynamic boundary layer becomes thinner and constrains the extent of the diffusion region, a scenario consistent with the model for axial segregation put forth by Burton, Prim, and Schlichter [69]. The simulation was stopped when the interface reached a position of  $z \approx 3.1$  due to accumulating error with time; however, we are confident that the profiles shown here are representative of the underlying model solution, aside from the spurious oscillations.

#### 4.3.4. Comparison to experimental axial profile

We desire to directly compare the results of the segregation

calculations presented in the prior section with the images obtained from the growth experiment. The neutron contrast images represent the effects of neutron attenuation due to absorption (dominated by europium) and scattering over their path of transit through the sample. The degree of attenuation (image darkness or contrast) thus depends upon the length of the path and the Eu concentration along that path. The contrast of each pixel of the meridional images shown in Fig. 2(a) has been adjusted to account for the path lengths across different chords through the ampoule of circular cross-section.

The contrast signal is also affected by variations in Eu concentration along each path, such as occur when there are radial variations in the concentration field, and transform techniques can be employed to extract more accurate contrast data under such conditions; see the approach described in [64]. However, we have found these effects to be relatively minor and have not accounted for them here.

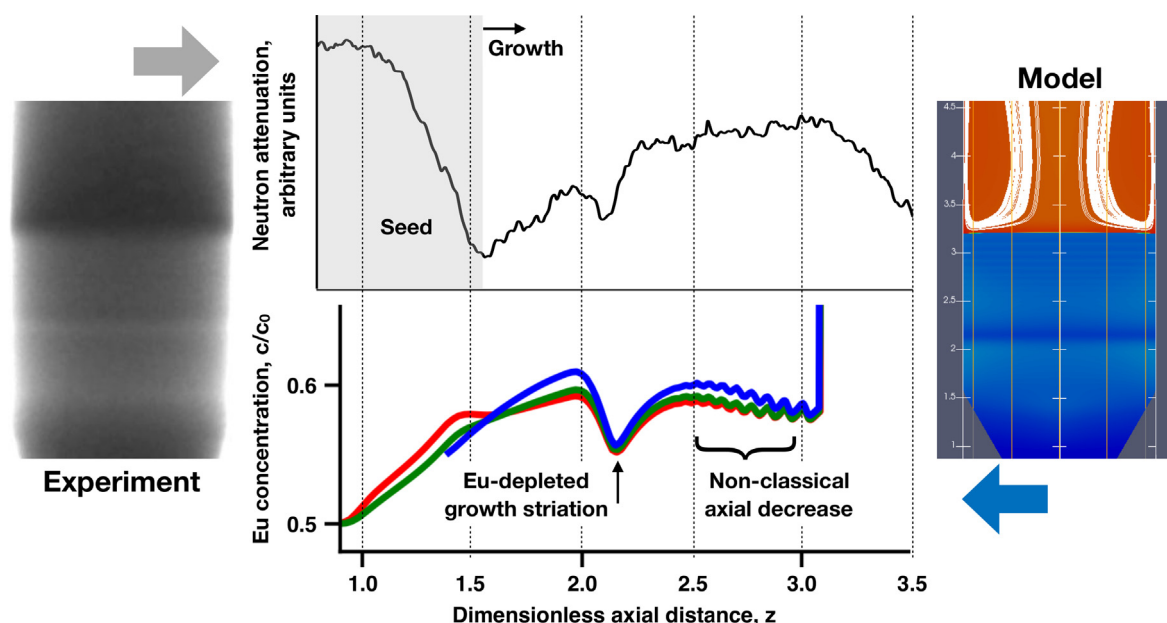
Finally, a more accurate mapping of contrast to europium concentration is possible using a nonlinear calibration curve, as described in Refs. [58,59,64]. Forgoing the intensive data processing required by this approach, we presume here that neutron attenuation is linearly proportional to europium concentration. For the Eu concentration field in the grown crystal, we estimate that this simplification results in calibration errors of less than 5%.

Fig. 8 presents a comparison between the Eu compositional fields observed in the experiment and our model predictions. The outer images present meridional cross sections through the crystal and melt after approximately 7 h of growth, with the left image showing the neutron contrast frame from the experiment and the right showing the Eu compositional field predicted by the CrysMAS-Cats2D model. In general, the observed and predicted distributions of europium through the solid match well, particularly the Eu-poor striation caused by the controller lock-up and growth pause.

A more detailed comparison is possible via the axial europium profiles along the system centerline shown by the images in the middle of Fig. 8. The upper image plots neutron attenuation (proportional to europium concentration) from the experiment, and the bottom shows predicted Eu concentration. Both profiles are plotted along the system centerline and as functions of dimensionless axial distance along the crystal. While the axial distance scale is identical for both profiles, there is some uncertainty regarding the origin of each axis due to the ambiguity of the actual time and position for the initiation of growth, as discussed in Section 4.1.

Considering the shape of the experimental profile, growth in the real system likely started at the indicated axial distance of  $z \approx 1.5$ , which differs from our assumption that  $z = 1.0$  marked the start of growth. We have indicated a shaded region on the upper plot to denote the initial, unmelted solid from which growth occurred. The distribution of Eu implied by the profile through this region is consistent with observations reported in Tremsin et al. [64], where image acquisition over a hold period preceding growth showed active diffusion of europium out of the seed and into the melt. Tremsin et al. [64] refer to this as a segregation-driven diffusion couple, in analogy with the classical diffusion couple used to measure solid-state diffusivities [105], and present an approach to estimate the solid-state diffusion and liquid-phase migration coefficients from the data acquired during the hold period. Similar solute diffusion between seed and melt has also been discussed as the origin of anomalous axial segregation in some systems [103].

From  $z \approx 1.5$  and onward, the observations and predictions are in very good qualitative agreement. The initial rise in Eu concentration during the initial growth transient is well represented, along with the dip in Eu concentration in the compositional striation caused by the growth pause. Finally, the non-classical decrease in axial concentration is also evident in both the experimental data and in the model prediction. While the growth simulation was halted due to the numerical issues discussed in the prior section, the neutron transmission profile from the experiment is shown for more of the grown crystal to emphasize the non-classical Eu axial profile.



**Fig. 8.** The europium (Eu) distribution is shown for the crystal grown in the VGF system. Outer images show two-dimensional representations of Eu after approximately 7 h of growth, via the neutron contrast image from the experiment on the left (darker areas correspond to higher concentration) and a visualization on the right from the CrysMAS–Cats2D model (using the color map provided in Fig. 6). The inner images show axial concentration profiles along the centerline resulting from Eu segregation during growth. The upper image shows neutron attenuation from the experiment, which is proportional to Eu concentration, and the lower image shows dimensionless Eu concentration predicted by the model. The grey area in the image above represents the initial seed from which growth is initiated. Both profiles show an initial transient during which the Eu concentration rises, a decreased-concentration band caused by the growth pause, and a non-classical decrease in axial Eu concentration as growth proceeds. (For interpretation of the references to colour in this figure legend, the reader is referred to the web version of this article.)

## 5. Conclusions

The neutron imaging studies of Tremsin et al. [58,59] were a remarkable diagnostic advance that allowed for the direct observation within a bulk crystal growth process. In this paper, we have applied computational models to predict the macroscopic transport of heat, mass, and momentum along with phase-change phenomena in the VGF crystal growth system employed in these neutron imaging experiments. Via the computational simulations, we have identified the underlying physical mechanisms that are responsible for several surprising experimental outcomes.

After an initial validation of thermal profiles in the VGF furnace, analysis via the CrysMAS heat transfer model provided a direct explanation of the solid/liquid interface shapes that were observed in the growth experiment. The evolution from an initially concave interface shape to convex during later stages of growth occurred due to significant changes in radial heat exchange between the ampoule and the surrounding furnace. For this VGF system, a reversal of radial heat flows occurred in different portions of the furnace. As the crystal was growing within the region surrounded by the conical ampoule holder, heat was flowing radially outward and the interface took on a concave shape. As the interface grew out of this region and into the cylindrical bore of the heated furnace zone, radial fluxes reversed, heat flowed into the ampoule near the interface, and the interface shape became convex.

The coupled, CrysMAS–Cats2D model provided for the additional capability of computing fluid flows within the melt, which then allowed for the analysis of europium transport and its segregation into the crystal. Due to the changing radial heat fluxes, described above in the discussion of solid/liquid interface shape, a surprisingly complicated, multiple-vortex flow was predicted to exist in this VGF system at early stages of growth. This flow structure was predicted to evolve as growth proceeded, with important consequences for Eu distribution with the grown crystal.

After tracking the initial transient in Eu distribution, the model

successfully predicted the compositional striation observed during the neutron imaging experiments. The striation resulted from a hold on furnace power due to controller lock-up, leading to a growth pause. While such an event would not be desired during a crystal growth production run, here it provided an excellent opportunity to affirm the mechanisms invoked by Tiller et al. [68] to explain “the presence of transverse bands [106] differing in concentration from the equilibrium value...created by rapid changes in the growth conditions of the crystal.”

As growth proceeded after the pause, the model predicted an increase in the axial concentration of europium, followed by a plateau and decrease. The axial Eu profile observed in the growth experiment was consistent with the model prediction. Notably, this behavior violates all classical theories for axial segregation, which predict a monotonically increasing concentration of Eu for this system [69,70,99]. The non-classical profile in this system evolved due to significant changes in the structure of the melt flow, whereby a multi-vortex flow was replaced by a single vortex. This resulted in a significant shrinking in the size of the diffusion layer,  $\delta$ , which caused the europium in the growing crystal to decrease, as explained via the use of different values for  $\delta$  in the BPS model [69]. Importantly, we would have no basis for understanding the non-classical axial concentration profiles observed in this VGF growth experiment without the detailed knowledge of flows states and europium transport in the melt provide by our model.

While the models employed here are powerful and rigorous, they are not necessarily easy to apply to describe the results of an actual growth experiment. In this study, significant effort was expended to validate the heat transfer model of the furnace and later to estimate physical properties of the BaBrCl:Eu system that were not known. Even after these efforts, our modeling results do not quantitatively match every aspect of the experiment. Nevertheless, we believe the agreement between model and observation is sufficient to provide an unambiguous understanding of the most important phenomena in this system and



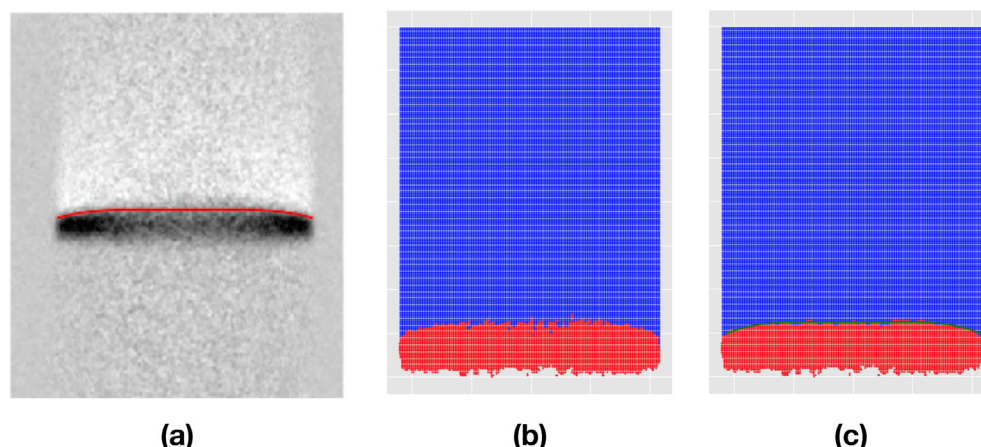


**Fig. 9.** The shape of the solid/liquid interface is extracted from the differential contrast images. (a) Image to be processed; red curve shows the extracted interface shape. (b) Pixels from the contrast image are classified by their greyscale value. Blue dots represent “melt class,” and red dots represent “solid class.” (c) Noise is removed from image (b) via the application of a K-nearest neighbors algorithm. The green line represents the detected interface (also shown by the red curve in image a). (For interpretation of the references to colour in this figure legend, the reader is referred to the web version of this article.)

how they have influenced growth outcomes.

As demonstrated in this paper, the synergy between powerful new diagnostic tools, such as the neutron imaging techniques presented here, and modeling provides for deeper and more fundamental understanding of bulk crystal growth processes. The continued development and use of these tools will provide a rigorous path forward for process optimization and control, accelerating the incremental advances that have, in the past, typically relied on empiricism, experience, and intuition. Ultimately, this will truly allow the closing of the loop between materials quality and process development for the growth of bulk, single crystals from the melt.

#### Appendix A. Extracting interface shape from neutron imaging data

A statistical method is employed to detect the solid/liquid interface shape from the differential contrast images. As discussed previously, the solid/liquid interface corresponds to the border separating the dark region and the light region above it. The dark region arises because the crystal grown between the images has a markedly lower Eu concentration than the melt from which it formed due to segregation. We desire to extract the shape of this interface from the strongly contrasting contrasts of the pixels in these images.

The image shown in Fig. 9(a) is used to provide sample data for the extraction algorithm. The first step is to read the greyscale of each pixel in the contrast image. Pixels with a greyscale higher than a threshold value (corresponding to the dark regions) are classified as the “solid class,” while those with a greyscale lower than the value (corresponding to the lighter regions) are classified as the “melt class”, as shown in Fig. 9(b).

The next step is to reduce the noise in the image to improve the accuracy of the extraction. “Noise” is defined as a spot of one class surrounded by the other class. The K-nearest neighbors algorithm from Scikit-learn library [107] is used to convert the outlier spot regions into the other class. Based on our experience, a neighbor number of 24 is sufficient to convert most “noise” spots and reliably predict the morphology of the solid-liquid interface. The processed, reduced-noise image is shown in Fig. 9(c).

The last step is to apply logistic regression to determine the solid/liquid interface, which is the decision boundary that separates the “melt class” and “solid class.” The following function is used to fit the interface shape:

$$z = a_1 * (r - r_0)^4 + a_2 * (r - r_0)^2 + a_3. \quad (4)$$

Here  $r$  is the radial coordinate,  $z$  is the axial coordinate,  $r_0$  is the radius position of the centerline, and  $a_1$ ,  $a_2$ ,  $a_3$  are coefficients to be determined by logistic regression. The searching of the boundary stops when a tolerance of  $1.0 \times 10^{-4}$  is reached. After the coefficients are obtained, the interface deflection and position are readily obtained; the detected interface shape for this image is shown by the green curve in Fig. 9(c) and the red curve in Fig. 9(a).

Every contrast frame is analyzed in this manner to extract interface shape and position. These experimental values were plotted as functions of time in Fig. 4.

#### References

- [1] P.W. Bridgman, Certain physical properties of single crystals of tungsten, antimony, bismuth, tellurium, cadmium, zinc, and tin, *Proc. Am. Acad. Arts Sci.* 60 (6) (1925) 305–383.
- [2] E.C. Kemble, F. Birch, Percy Williams Bridgman, 1882–1961: A Biographical Memoir, National Academy of Sciences, 1970.
- [3] R.S. Feigelson, Crystal growth through the ages: a historical perspective, 2nd ed., in: T. Nishinaga (Ed.), *Handbook of Crystal Growth*, vol. I, Part A, Elsevier, 2015, pp. 1–84 Ch. 1.
- [4] G. Tammann, *Metallography: Chemistry and physics of the metals and their alloys*, Translated by R.S. Dean and L.G. Swenson, The Chemical Catalog Company, Inc., 1925.
- [5] J. Obreimov, L. Schubnikov, *Z. Phys.* 25 (1924) 31.
- [6] D.C. Stockbarger, The production of large single crystals of lithium fluoride, *Rev. Sci. Instrum.* 7 (1936) 133.
- [7] A. Murgai, H. Gatos, A. Witt, Quantitative analysis of microsegregation in silicon grown by the Czochralski method, *J. Electrochem. Soc.* 123 (1976) 224–229.
- [8] K.M. Kim, A.F. Witt, M. Lichtensteiger, H.C. Gatos, Quantitative analysis of the effects of destabilizing vertical thermal gradients on crystal growth and segregation: Ga-doped Ge, *J. Electrochem. Soc.* 125 (1978) 475–480.
- [9] L.O. Wilson, The effect of fluctuating growth rates on segregation in crystals grown from the melt: I. No backmelting, *J. Cryst. Growth* 48 (3) (1980) 435–450.
- [10] C. Wang, J. Carruthers, A. Witt, Growth rate dependence of the interface distribution coefficient in the system Ge-Ga, *J. Cryst. Growth* 60 (1) (1982) 144–146.

- [11] C.A. Wang, A.F. Witt, J.R. Carruthers, Analysis of crystal growth characteristics in a conventional vertical Bridgman configuration, *J. Cryst. Growth* 66 (1984) 299–308.
- [12] N. Abrosimov, A. Lüdge, H. Riemann, W. Schroeder, Lateral photovoltage scanning (LPS) method for the visualization of the solid–liquid interface of Si<sub>1-x</sub>Ge<sub>x</sub> single crystals, *J. Cryst. Growth* 237–239 (2002) 356–360.
- [13] C.A. Wang, *Crystal growth and segregation in vertical Bridgman configuration*, Ph.D. thesis, Massachusetts Institute of Technology, 1984.
- [14] K. Hjelt, M. Juvonen, T. Tuomi, S. Nenonen, E.E. Eissler, M. Bavdaz, Photoluminescence of Cd<sub>1-x</sub>Zn<sub>x</sub>Te crystals grown by high-pressure Bridgman technique, *Phys. Status Solidi (a)* 162 (1997) 747–763.
- [15] N. Zhang, A. Yeckel, A. Burger, Y. Cui, K. Lynn, J.J. Derby, Anomalous segregation during electrodynamic gradient freeze growth of cadmium zinc telluride, *J. Cryst. Growth* 325 (2011) 10–19.
- [16] Y. Huang, W.J. Debnam, A.J. Fripp, Interface shapes during vertical Bridgman growth of (Pb, Sn)Te crystals, *J. Cryst. Growth* 104 (1990) 315–326.
- [17] U.N. Roy, S. Weiler, J. Stein, Growth and interface study of 2 in diameter CdZnTe by THM technique, *J. Cryst. Growth* 312 (19) (2010) 2840–2845.
- [18] H. Potts, W.R. Wilcox, Thermal fields in the bridgman-Stockbarger technique, *J. Cryst. Growth* 73 (2) (1985) 350–358.
- [19] G.T. Neugebauer, W.R. Wilcox, Convection in the vertical Bridgman-Stockbarger technique, *J. Cryst. Growth* 89 (2) (1988) 143–154.
- [20] N. Singh, M. Gottlieb, T. Henningsen, R. Hopkins, R. Mazelsky, M. Glicksman, S. Coriell, G. Santoro, W. Duval, Growth and characterization of lead bromide crystals, *J. Cryst. Growth* 123 (1) (1992) 221–226.
- [21] C. Lan, D. Yang, C. Ting, F. Chen, A transparent multizone furnace for crystal growth and flow visualization, *J. Cryst. Growth* 142 (1994) 373–378.
- [22] C.W. Lan, C.C. Ting, A study on the interface control of vertical Bridgman crystal growth using a transparent multizone furnace, *Chem. Eng. Commun.* 145 (1) (1996) 131–143.
- [23] C. Lan, C. Song, Growth of benzil crystals by vertical dynamic gradient freeze technique in a transparent furnace, *J. Cryst. Growth* 180 (1) (1997) 127–135.
- [24] C. Batur, A. Srinivasan, W.M.B. Duval, N.B. Singh, D. Golovaty, On-line control of solid-liquid interface by state feedback, *J. Cryst. Growth* 205 (1999) 395–409.
- [25] R.G. Seidensticker, W.R. Rosch, R. Mazelsky, R.H. Hopkins, N.B. Singh, S.R. Coriell, W.M.B. Duval, C. Batur, Active control of interface shape during the crystal growth of lead bromide, *J. Cryst. Growth* 198 (1999) 988–994.
- [26] S.C. Bates, K.S. Knight, Auxiliary optical heating for controlled crystal growth, *J. Cryst. Growth* 240 (1) (2002) 277–286.
- [27] K.T. Zawilski, M. Claudia, C. Custodio, R.C. DeMattei, R.S. Feigelson, Vibroconvective mixing applied to vertical bridgman growth, *J. Cryst. Growth* 258 (1) (2003) 211–222.
- [28] N. Balamurugan, A. Arulchakkaravarthi, P. Ramasamy, Growth of 2,5-diphenylloxazole-doped naphthalene crystal by Bridgman method and its fluorescence studies, *J. Cryst. Growth* 310 (7) (2008) 2115–2119.
- [29] F. Barvinschi, A. Stanculescu, F. Stanculescu, Heat transfer process during the crystallization of benzil grown by the Bridgman-Stockbarger method, *J. Cryst. Growth* 317 (1) (2011) 23–27.
- [30] A. Ostrogorsky, V. Riabov, N. Dropka, Interface control by rotating submerged heater/baffle in vertical Bridgman configuration, *J. Cryst. Growth* 498 (2018) 269–276.
- [31] S.C. Bates, *Transparent furnaces for high temperature research*, Tech. rep., NASA Tech Briefs, 1998.
- [32] 1200° C Transparent Laboratory Furnace, Thoughtventions Unlimited LLC. <http://www.tvu.com/FEHTTF.html>.
- [33] L. Stand, M. Zhuravleva, J. Johnson, M. Koschan, Y. Wu, S. Donald, K. Vaigneur, E. Lukosi, C. Melcher, Exploring growth conditions and Eu<sup>2+</sup> concentration effects for K<sub>2</sub>Sr<sub>2</sub>Eu: Eu scintillator crystals II: 25 mm crystals, *J. Cryst. Growth* 483 (2018) 301–307.
- [34] L. Stand, M. Zhuravleva, B. Chakoumakos, J. Johnson, M. Loyd, Y. Wu, M. Koschan, C. Melcher, Crystal growth and scintillation properties of Eu<sup>2+</sup> doped Cs<sub>2</sub>CaF<sub>6</sub> and Cs<sub>2</sub>SrF<sub>6</sub>, *J. Cryst. Growth* 486 (2018) 162–168.
- [35] S. Lam, C. Gugushev, A. Burger, M. Hackett, S. Motakef, Crystal growth and scintillation performance of Cs<sub>2</sub>HfCl<sub>6</sub> and Cs<sub>2</sub>HfCl<sub>4</sub>Br<sub>2</sub>, *J. Cryst. Growth* 483 (2018) 121–124.
- [36] J.-I. Chikawa, Technique for the video display of x-ray topographic images and its application to the study of crystal growth, *J. Cryst. Growth* 24–25 (1974) 61–68.
- [37] G. Grange, C. Jourdan, A.L. Coulet, J. Gastaldi, Observation of the melting–solidification process of an Al crystal by synchrotron x-ray topography, *J. Cryst. Growth* 72 (1985) 748–752.
- [38] P.G. Barber, R.K. Crouch, A.L. Fripp, W.J. Debnam, R.F. Berry, R. Simchick, A procedure to visualize the melt–solid interface in Bridgman grown germanium and lead tin telluride, *J. Cryst. Growth* 74 (1) (1986) 228–230.
- [39] S. Ozawa, T. Fukuda, In-situ observation of lec gas solid-liquid interface with newly developed x-ray image processing system, *J. Cryst. Growth* 76 (2) (1986) 323–327.
- [40] K. Kakimoto, M. Eguchi, H. Watanabe, T. Hibiya, In-situ observation of solid-liquid interface shape by X-ray radiography during silicon single crystal growth, *J. Cryst. Growth* 91 (4) (1988) 509–514.
- [41] K. Kakimoto, M. Eguchi, H. Watanabe, T. Hibiya, Direct observation by X-ray radiography of convection of molten silicon in the Czochralski growth method, *J. Cryst. Growth* 88 (3) (1988) 365–370.
- [42] K. Kakimoto, M. Eguchi, H. Watanabe, T. Hibiya, Direct observation by X-ray radiography of convection of boric oxide in the GaAs liquid encapsulated Czochralski growth, *J. Cryst. Growth* 94 (2) (1989) 405–411.
- [43] K. Kakimoto, M. Eguchi, H. Watanabe, T. Hibiya, Natural and forced convection of molten silicon during Czochralski single crystal growth, *J. Cryst. Growth* 94 (2) (1989) 412–420.
- [44] K. Kakimoto, M. Eguchi, H. Watanabe, T. Hibiya, Flow instability of molten silicon in the Czochralski configuration, *J. Cryst. Growth* 102 (1) (1990) 16–20.
- [45] K. Kakimoto, M. Eguchi, H. Watanabe, T. Hibiya, In-situ observation of impurity diffusion boundary layer in silicon Czochralski growth, *J. Cryst. Growth* 99 (1, Part 2) (1990) 665–669.
- [46] K. Kakimoto, M. Eguchi, T. Hibiya, In-situ monitoring of dopant concentration variation in a silicon melt during Czochralski growth, *J. Cryst. Growth* 112 (4) (1991) 819–823.
- [47] M. Watanabe, M. Eguchi, K. Kakimoto, T. Hibiya, Double-beam X-ray radiography system for three-dimensional flow visualization of molten silicon convection, *J. Cryst. Growth* 133 (1) (1993) 23–28.
- [48] Y. Wang, K. Kakimoto, Crystal–melt interface shape and dislocations during the melting of silicon, *J. Cryst. Growth* 247 (1–2) (2003) 1–12.
- [49] T. Campbell, J. Koster, Visualization of liquid–solid interface morphologies in gallium subject to natural convection, *J. Cryst. Growth* 140 (3–4) (1994) 414–425.
- [50] T. Campbell, J. Koster, Radioscopic visualization of indium antimonide growth by the vertical Bridgman-Stockbarger technique, *J. Cryst. Growth* 147 (3–4) (1995) 408–410.
- [51] T. Campbell, J. Koster, A novel vertical Bridgman-Stockbarger crystal growth system with visualization capability, *Meas. Sci. Technol.* 6 (5) (1995) 472–476.
- [52] J. Koster, Visualization of convective flow in liquid metals, *Am. Soc. Mech. Eng. Heat Transf. Division*, (Publication) HTD 350 (1997) 15–22.
- [53] J. Koster, T. Seidel, R. Derbail, A radioscopic technique to study convective fluid dynamics in opaque liquid metals, *J. Fluid Mech.* 343 (1997) 29–41.
- [54] J. Koster, R. Derbail, A. Grötzbach, Visualization of convective solidification in a vertical layer of eutectic Ga–In melt, *Appl. Phys. A: Mater. Sci. Process.* 64 (1) (1997) 45–54.
- [55] R. Derbail, J. Koster, Visualization study of melting and solidification in convecting hypoeutectic Ga–In alloy, *Int. J. Heat Mass Transf.* 41 (16) (1998) 2537–2548.
- [56] J. Koster, Directional solidification and melting of eutectic GaIn, *Cryst. Res. Technol.* 34 (9) (1999) 1129–1140.
- [57] P. Pernot, B. Gorges, H. Vitoux, R. Kluender, F. Masiello, J. Baruchel, A furnace for coherent beam transmission topography applied to ferroelectric crystals, *Physica Status Solidi (A) Appl. Mater. Sci.* 206 (8) (2009) 1880–1883.
- [58] A.S. Tremsin, M.G. Makowska, D. Perrodin, T. Shalapska, I.V. Khodyuk, P. Trtik, P. Boillat, S.C. Vogel, A.S. Losko, M. Strobl, L.T. Kuhna, G.A. Bizarri, E.D. Bourret-Courchesne, In situ diagnostics of the crystal-growth process through neutron imaging: application to scintillators, *J. Appl. Crystallogr.* 49 (2016) 743–755.
- [59] A.S. Tremsin, D. Perrodin, A.S. Losko, S.C. Vogel, M.A.M. Bourke, G.A. Bizarri, E.D. Bourret-Courchesne, Real-time crystal growth visualization and quantification by energy-resolved neutron imaging, *Sci. Rep.* 7 (46275) (2017) 1–9.
- [60] A.S. Tremsin, High resolution neutron counting detectors with microchannel plates and their applications in neutron radiography, diffraction and resonance absorption imaging, *Neutron News* 23 (2012) 35–38.
- [61] A.S. Tremsin, J.V. Vallerger, J.B. McPhate, O.H.W. Siegmund, Optimization of high count rate event counting detector with microchannel plates and quad timepix readout, *Nucl. Instr. Meth. A* 787 (2015) 20–25.
- [62] G. Gundiah, Z. Yan, G. Bizarri, S.E. Derenzo, E.D. Bourret-Courchesne, Structure and scintillation of Eu<sup>2+</sup>-activated BaBrCl and solid solutions in the BaCl<sub>2</sub>–BaBr<sub>2</sub> system, *J. Luminescence* 138 (2013) 143–149.
- [63] A.S. Tremsin, D. Perrodin, A.S. Losko, S.C. Vogel, T. Shinohara, K. Oikawa, J.H. Peterson, C. Zhang, J.J. Derby, A. Zlokapa, G.A. Bizarri, E.D. Bourret, In-situ observation of phase separation during growth of Cs<sub>2</sub>LiLaBr<sub>6</sub>: Ce using energy-resolved neutron imaging, *Cryst. Growth Des.* 17 (12) (2017) 6372–6381.
- [64] A.S. Tremsin, D. Perrodin, A.S. Losko, S.C. Vogel, T. Shinohara, K. Oikawa, G.A. Bizarri, E.D. Bourret, J.H. Peterson, K.P. Wang, J.J. Derby, In-situ observation and analysis of solid-state diffusion and liquid migration in a crystal growth system: a segregation-driven diffusion couple, *Acta Mater.* 186 (2020) 434–442.
- [65] D.R. Onken, R.T. Williams, D. Perrodin, T. Shalapska, E.D. Bourret, A.S. Tremsin, S.C. Vogel, Crystal structure evolution of BaBrCl and BaBrCl:5% Eu up to 1073 K by neutron diffraction, *J. Appl. Crystallogr.* 51 (2) (2018) 498–504.
- [66] C. Zhang, *Analyses of the growth of BaBrCl:Eu*, Ph.D. thesis University of Minnesota, 2020.
- [67] C. Zhang, B. Gao, A.S. Tremsin, D. Perrodin, T. Shalapska, E.D. Bourret, D.R. Onken, S.C. Voge, J.J. Derby, Analysis of chemical stress and the propensity for cracking during the vertical Bridgman growth of BaBrCl:Eu, *J. Crystal Growth*, 2020, in preparation.
- [68] W.A. Tiller, K.A. Jackson, J.W. Rutter, B. Chalmers, The redistribution of solute atoms during the solidification of metals, *Acta Metall.* 1 (1953) 428.
- [69] J.A. Burton, R.C. Prim, W.P. Slichter, The distribution of solute in crystals grown from the melt. Part I. Theoretical, *J. Chem. Phys.* 21 (1953) 1987–1991.
- [70] V.G. Smith, W.A. Tiller, J.W. Rutter, A mathematical analysis of solute redistribution during solidification, *Canadian J. Phys.* 33 (1955) 723–745.
- [71] M.C. Flemings, *Solidification Processes*, McGraw-Hill Inc, New York, 1974.
- [72] R.A. Brown, Theory of transport processes in single crystal growth from the melt, *AIChE J.* 34 (6) (1988) 881–911.
- [73] K.A. Jackson, Constitutional supercooling surface roughening, *J. Cryst. Growth* 264 (2004) 519–529.
- [74] J.J. Derby, Macroscopic transport processes during the growth of single crystals from the melt, in: J. van der Eerden, O. Bruinsma (Eds.), *Science and Technology of Crystal Growth*, Kluwer Academic Publishers, Dordrecht, The Netherlands, 1995, pp. 97–110.
- [75] A. Yeckel, J.J. Derby, Computational simulations of the growth of crystals from

- liquids, in: H. Scheel, T. Fukuda (Eds.), *Crystal Growth Technology*, John Wiley & Sons, West, Sussex, UK, 2003, pp. 115–137 Ch. 6.
- [76] A. Yeckel, J.J. Derby, Computer modelling of bulk crystal growth, in: P. Capper, A. Willoughby, S. Kasap (Eds.), *Bulk Crystal Growth of Electronic, Optical, and Optoelectronic Materials*, John Wiley & Sons, West Sussex, UK, 2005, pp. 73–119.
- [77] J.J. Derby, A. Yeckel, Heat transfer analysis and design for bulk crystal growth: perspectives on the Bridgman method, 2nd ed., in: T. Nishinaga, P. Rudolph (Eds.), *Handbook of Crystal Growth*, vol. II, Part A, Elsevier, 2015, pp. 793–843 Ch. 20.
- [78] J.J. Derby, Fluid dynamics in crystal growth: the good, the bad, and the ugly, *Prog. Cryst. Growth Charact. Mater.* 62 (2016) 286–301.
- [79] M.R.H. Kurz, Development of CrysVUn + +, a software system for numerical modelling and control of industrial growth processes, Ph.D. thesis, Universität Erlangen - Nürnberg, 1998.
- [80] M. Kurz, A. Pusztai, G. Müller, Development of a new powerful computer code CrysVUN + + especially designed for fast simulation of bulk crystal growth processes, *J. Cryst. Growth* 198 (1999) 101–106.
- [81] R. Backofen, M. Kurz, G. Müller, Process modeling of the industrial VGF growth process using the software package CrysVUN + +, *J. Cryst. Growth* 211 (2000) 202–206.
- [82] J. Fainberg, D. Vizman, J. Friedrich, G. Müller, A new hybrid method for the global modeling of convection in CZ crystal growth configurations, *J. Cryst. Growth* 303 (1) (2007) 124–134.
- [83] CrysMAS user manual and tutorial, 2013. <http://www.cgl-erlangen.com/downloads/Manual.pdf>.
- [84] A. Yeckel, R.T. Goodwin, Cats2D (crystallization and Transport Simulator), User Manual, 2003, unpublished, <http://www.cats2d.com>.
- [85] A. Pandey, A. Yeckel, M. Reed, C. Szeles, M. Hainke, G. Müller, J.J. Derby, Analysis of the growth of cadmium zinc telluride in an electrodynamic gradient freeze furnace via a self-consistent, multi-scale numerical model, *J. Cryst. Growth* 276 (2005) 133–147.
- [86] A. Yeckel, A. Pandey, J.J. Derby, Fixed-point convergence of modular, steady-state heat transfer models coupling multiple scales and phenomena for melt-crystal growth, *Int. J. Numer. Methods Eng.* 67 (2006) 1768–1789.
- [87] A. Yeckel, L. Lun, J.J. Derby, An approximate block Newton method for coupled iterations of nonlinear solvers: Theory and conjugate heat transfer applications, *J. Comput. Phys.* 228 (2009) 8566–8588.
- [88] A. Yeckel, L. Lun, J.J. Derby, Multi-scale crystal growth computations via an approximate block Newton method, *J. Cryst. Growth* 312 (2010) 1463–1467.
- [89] W.M. Deen, *Analysis of Transport Phenomena*, second ed., Oxford University Press, 2012 Ch. 12, pp. 467–468.
- [90] E.D. Bourret-Courchesne, G.A. Bizarri, G.R. Borade, R., E.C. Samulon, Z. Yan, S.E. Derenzo, Crystal growth and characterization of alkali-earth halide scintillators, *J. Cryst. Growth* 352 (1) (2012) 78–83.
- [91] Z. Yan, T. Shalapska, E.D. Bourret, Czochralski growth of the mixed halides BaBrCl and BaBrCl:Eu, *J. Cryst. Growth* 435 (2016) 42–45.
- [92] A. Dworkin, M. Bredig, The heat of fusion of the alkali metal halides, *J. Phys. Chem.* 64 (1960) 269–272.
- [93] K. McCarthy, S. Ballard, Thermal conductivity of eight halide crystals in the temperature range 220 K to 390 K, *J. Appl. Phys.* 31 (8) (1960) 1410–1412.
- [94] G. Janz, R. Tomkins, C. Allen, J.J.R. Downey, G. Gardner, U. Krebs, S. Singer, Molten salts: Volume 4, part 2, chlorides and mixtures, electrical conductance, density, viscosity, and surface tension data, *J. Phys. Chem. Reference Data* 4 (4) (1975).
- [95] G. Janz, Thermal dynamic and transport properties of molten salts: Correlation equations for critically evaluated density, surface tension, electric conductance, and viscosity data, *J. Phys. Chem. Reference Data* 17 (Supplement No. 2) (1988).
- [96] J.M.W. Chase, NIST-JANAF Thermalchemical Tables, Fourth Edition, *J. Phys. Chem. Reference Data*, Monograph 9 (Part I and Part II) (1988) 1963.
- [97] C.E. Chang, W.R. Wilcox, Control of interface shape in the vertical Bridgman-Stockbarger technique, *J. Cryst. Growth* 21 (1) (1974) 135–140.
- [98] J.H. Peterson, J.J. Derby, An axial temperature profile curvature criterion for the engineering of convex crystal growth interfaces in Bridgman systems, *J. Cryst. Growth* 468 (2017) 899–904.
- [99] E. Scheil, Bemerkungen zur schichtkristallbildung, *Z. Metallk.* 34 (1942) 70.
- [100] C.J. Chang, R.A. Brown, Radial segregation induced by natural convection and melt/solid interface shape in vertical Bridgman growth, *J. Cryst. Growth* 63 (1983) 343.
- [101] J. Garandet, On the problem of radial segregation in an idealized horizontal Bridgman configuration: scaling and numerical approaches, *J. Cryst. Growth* 114 (4) (1991) 593–602.
- [102] J.P. Garandet, J.J. Favier, D. Camel, Segregation phenomena in crystal growth from the melt, in: D. Hurlé (Ed.), *Bulk Crystal Growth: Growth Mechanisms and Dynamics*, Handbook of Crystal Growth, vol. 2B, Elsevier Science B.V., 1994, Ch. 12, pp. 659–708.
- [103] S. Kuppuraio, S. Brandon, J.J. Derby, Modeling the vertical Bridgman growth of cadmium zinc telluride. II. Transient analysis of zinc segregation, *J. Cryst. Growth* 155 (1995) 103–111.
- [104] Q. Xiao, S. Kuppuraio, A. Yeckel, J.J. Derby, On the effects of ampoule tilting during vertical Bridgman growth: three-dimensional computations via a massively parallel, finite element model, *J. Cryst. Growth* 167 (1996) 292–304.
- [105] A. Kodentsov, A. Paul, Diffusion couple technique: a research tool in materials science, in: A. Paul, S. Divinski (Eds.), *Handbook of Solid State Diffusion: Diffusion Analysis in Material Applications*, vol. 2, Elsevier Inc, 2017, pp. 207–275.
- [106] M.T. Stewart, R. Thomas, K. Wauchope, W.C. Winegard, B. Chalmers, New segregation phenomena in metals, *Phys. Rev.* 83 (1951) 657.
- [107] F. Pedregosa, G. Varoquaux, A. Gramfort, V. Michel, B. Thirion, O. Grisel, M. Blondel, P. Prettenhofer, R. Weiss, V. Dubourg, J. Vanderplas, A. Passos, D. Cournapeau, M. Perrot, E. Duchesnay, Scikit-learn: machine learning in Python, *J. Mach. Learn. Res.* 12 (2011) 2825–2830.